PCCP

RSC Publishing

PAPER

Mechanisms of nanoparticle formation by ultra-short laser ablation of metals in liquid environment†

Cite this: *Phys. Chem. Chem. Phys.*, 2013, **15**, 3108

Mikhail E. Povarnitsyn,*[ab] Tatiana E. Itina,[c] Pavel R. Levashov[ab] and Konstantin V. Khishchenko[ab]

Received 31st July 2012,
Accepted 6th December 2012

DOI: 10.1039/c2cp42650a

www.rsc.org/pccp

Laser ablation in liquids is now commonly used to produce colloidal nanoparticles (NPs) that have found numerous applications in different areas. In experiments, NPs of different materials can be rather easily obtained by using laser systems with various pulse durations, shapes, wavelengths, and fluences. In this paper, we focus our attention on metal (gold) NPs produced by ultra-short laser pulses. To better understand the mechanisms of the NPs formation, we perform modeling of femtosecond laser interactions with a gold target in the presence of liquid (water). Simulation of the ablation process over several nanoseconds shows that most of the primary NPs originate from the ablated metastable liquid layer, whereas only a minority is formed by condensation inside the cavitation bubble. These particles will further grow/evaporate, and coagulate during a much longer collision stage in the liquid colloid.

1 Introduction

Nanoparticles (NPs) of different materials have found numerous applications due to their unique properties.[1,2] For instance, particular attention has been attracted to several very promising medical applications, such as cancer and antibacterial treatment, imaging, censors, *etc.* Therefore, new methods are required to prepare liquid solutions with NPs using ultra-short and long laser pulses.[3–8] Laser ablation (LA) is one such simple and versatile technique. The major advantage of the LA method is in its ''green'' character, which means that NPs are almost unaffected chemically. Even when some surfactant molecules are introduced to liquid solutions, the chemical properties of NPs surface stay mostly unchanged. This advantage, as well as a possibility of control of NP size by changing laser parameters or liquid composition, makes LA a unique tool for future NP synthesis. Despite the evident attractiveness of the LA technique, the mechanisms involved in NP formation are far from being understood. In fact, many studies have revealed an interplay between different physical and chemical processes involved in NP synthesis.[9–13] For instance, it was demonstrated that laser ablation in liquids is accompanied by the formation of shock waves and a cavitation bubble. Some groups then investigated this primary stage of NP formation, whereas other groups considered effects taking place later, after the bubble collapse in the liquid colloid. Among the processes occurring later, fragmentation and coagulation were shown to be particularly important.[14,15] In addition, the roles of electrostatic interactions and chemical processes were underlined. In this paper we focus our attention on the primary mechanisms of NP formation. We consider the very early ablation stage (several nanoseconds), which provides initial conditions for much longer later processes. At this primary stage, the ablation process is difficult to observe experimentally, and most of the experimental information concerning NP formation is obtained at much longer delays than the ones considered in this paper. Our aim is to shed light on the mechanisms of ultra-short laser ablation in the presence of liquid, and to answer the following questions: (i) are these mechanisms different from those in vacuum? (ii) can they lead to the formation of nanoparticles? (iii) is condensation in a cavitation bubble possible, or do other effects explain primary NP formation? To answer these questions, we perform a detailed simulation based on two-temperature hydrodynamics with realistic equations of state (EOS). We choose gold as the target material because of its multiple applications, and water since this liquid is widely used in experiments as an ambient medium with well elaborated EOS. The obtained results contain the information about the time-varying phase states in the target, phase trajectories of different target layers and space distribution of thermodynamic

[a] *Joint Institute for High Temperatures RAS, Izhorskaya 13 Bldg 2, Moscow 125412, Russia. E-mail: povar@ihed.ras.ru*
[b] *Moscow Institute of Physics and Technology (State University), Institutsky lane 9, Dolgoprudny, Moscow region 141700, Russia*
[c] *Laboratoire Hubert Curien, 18 rue Benoît Lauras, Bât. F, 42000, St-Etienne, France*

† This article was submitted following the Laser Ablation and Nanoparticle Generation in Liquids (ANGEL 2012) Conference.

This journal is © the Owner Societies 2013

parameters. The performed analysis clarifies the roots of primary NP formation and interprets several experimental observations. In particular, we can explain the existence of a rather narrow fluence window that should be applied to obtain primary NPs. The paper is organized as follows. First, we describe our model and modifications that have been done to account for liquid environment. Then, we present the calculation results obtained for a single femtosecond laser pulse with different laser fluences. Finally, we focus our attention on the analysis of early stages of laser ablation into liquid, phase trajectories, and discuss the role of different phase states in NP formation.

2 Model and calculation details

For description of initial stages of the target response on laser irradiation in presence of ambient liquid, we apply a 1D Lagrangian two-temperature hydrodynamic model.[16] The advantages of this approach are the possibility to model several materials simultaneously, explicit tracking of interfaces and free surfaces, non-uniform mesh usage and treatment of spallation in solid and liquid phases based on a nucleation model. Various 3D effects, such as self-focusing, refraction, dielectric breakdown[17] and laser beam propagation through the liquid,[18] are out of the scope of this article. Instead, we specify the intensity of the laser light at the target surface (already after propagation through the water layer) and call it simply *local laser intensity*. Note that the local intensity may be higher than the incident one because of the tightly focused beam and self-focusing effect[18] *etc.*

The basic hydrodynamic equations for both metal and liquid are written in the form of conservation laws for mass, momentum and energy of electron and ion subsystems as follows

$$\frac{\partial(1/\rho)}{\partial t} - \frac{\partial u}{\partial m} = 0, \tag{1}$$

$$\frac{\partial u}{\partial t} + \frac{\partial(P_\mathrm{i} + P_\mathrm{e})}{\partial m} = 0, \tag{2}$$

$$\frac{\partial e_\mathrm{e}}{\partial t} + P_\mathrm{e}\frac{\partial u}{\partial m} = -\gamma_\mathrm{ei}(T_\mathrm{e} - T_\mathrm{i})/\rho + Q_\mathrm{L}/\rho + \frac{\partial}{\partial m}\left(\rho\kappa_\mathrm{e}\frac{\partial T_\mathrm{e}}{\partial m}\right), \tag{3}$$

$$\frac{\partial e_\mathrm{i}}{\partial t} + P_\mathrm{i}\frac{\partial u}{\partial m} = \gamma_\mathrm{ei}(T_\mathrm{e} - T_\mathrm{i})/\rho. \tag{4}$$

In these equations ρ is the material density; t is the time; m is the mass coordinate ($\mathrm{d}m = \rho\mathrm{d}z$); z is the space coordinate; u is the hydrodynamic velocity (single-fluid approximation); P_e and P_i are the pressures of electrons and ions, respectively; e_e and e_i are the specific energies of electrons and ions, respectively; $\gamma_\mathrm{ei}(\rho,T_\mathrm{i},T_\mathrm{e})$ is the electron–ion energy coupling factor; T_e and T_i are the temperatures of electrons and ions, respectively. The laser energy absorption by the conduction-band electrons in the target is taken into account by the source term $Q_\mathrm{L}(t,z)$ which is calculated on time-dependent profile of complex dielectric constant $\varepsilon(\rho,T_\mathrm{i},T_\mathrm{e},\omega_\mathrm{L})$ using a transfer-matrix method.[16,19] For simulation of optical, transport and thermodynamic properties of gold we use wide-range models. The model of complex permittivity for gold is similar to that described elsewhere.[20] It depends on the laser frequency ω_L and has asymptotic limits for the normal[21] and ideal hot plasma state.[22] The wide-range coefficient of electron thermal conductivity $\kappa_\mathrm{e}(\rho,T_\mathrm{i},T_\mathrm{e})$ is used for the description of heat transport. The model of the heat conduction coefficient is similar to that described in our previous work[20] and the temperature dependence for gold is adjusted to meet theoretical calculations.[23] The coupling factor model[20] is fitted to satisfy available first-principle findings.[24]

Finally, for the description of thermodynamic properties of gold, we add the relations of the form $P_\mathrm{e}(\rho,T_\mathrm{e})$, $P_\mathrm{i}(\rho,T_\mathrm{i})$, $e_\mathrm{e}(\rho,T_\mathrm{e})$, $e_\mathrm{i}(\rho,T_\mathrm{i})$ known from the two-temperature multi-phase EOS with the Thomas–Fermi expression for the thermal contribution of electrons.[25] The phase diagram of gold in temperature–density coordinates obtained from the EOS is presented in Fig. 1. Using multi-phase EOS we account for thermodynamic properties of the target material in different phase states and resolve the phase transitions such as melting and evaporation. The presence of metastable states in the EOS (see Fig. 1) gives us an opportunity to introduce into hydrodynamics the kinetic models of nucleation[26,27] which control the life time of these metastable states. In particular, according to these models the life time of the metastable liquid state [region (l) in Fig. 1] drastically drops to zero when approaching the spinodal while in the vicinity of the binodal it tends to infinity.

In the present simulation we neglect the optical and transport properties of water in comparison with the gold ones, and thus treat water as a transparent (ε = 4.4) and heat-insulating (κ_e = 0) substance. However, the mechanical properties of water are essential for proper reduction of gold target expansion (in comparison with ablation into vacuum), and they are described

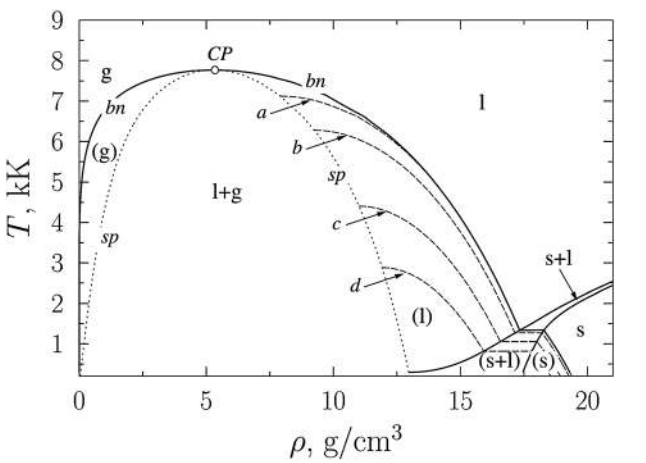

Fig. 1 Temperature–density phase diagram of gold with phase states: s—solid; l—liquid; g—gas; l + g—liquid–gas mixture; s + l—melting; (s)—metastable solid; (s + l)—metastable melting; (l)—metastable liquid; (g)—metastable gas. *CP* is the critical points, *bn* and *sp* are binodal and spinodal curves, respectively. Dashed lines show isobars in metastable liquid phase: *a*—0 GPa; *b*—−1 GPa; *c*—−4 GPa; *d*—−7 GPa.

by a single-phase caloric EOS[28] defined by the dependence of the form $P(\rho,e)$, where $P = P_i + P_e$ is the full pressure, and $e = e_i + e_e$ is the full specific energy. The water EOS describes well the shock Hugoniot data up to 100 GPa.[29,30] The water–gold interface is explicitly resolved thanks to the Lagrangian formulation of the conservation laws (1)–(4).

3 Simulation results and discussion

In this section we simulate a single pulse LA of thick gold target into water. Initially, the water–gold interface is located at $z = 0$ and the water layer of 100 μm thickness is placed at $z < 0$ while the gold target at $z > 0$ and has 100 μm thickness. The thicknesses of the water and gold layers are chosen so that the shock wave reflection from the free surfaces do not produce any disturbance in the area of interest during the simulation. The laser pulse wavelength is 800 nm, which corresponds to the first harmonic of the Ti : sapphire laser set-up; the temporal pulse shape is $I(t) = I_0\exp[-\ln(16)t^2/\tau^2]$, where I_0 is the local peak intensity and $\tau = 200$ fs is the full width at half maximum. We apply several local peak intensities: $I_0 = 1; 2; 3; 4; 5 \times 10^{13}$ W cm^{-2} to explore different regimes of the LA in water for time interval -1 ps $\leq t \leq 10$ ns. For the local laser intensity of $I_0 = 1 \times 10^{13}$ W cm^{-2} (absorbed fluence $F_{abs} = 0.032$ J cm^{-2}) we do not observe even melting on the surface of the target. When the local peak intensity is $I_0 = 2 \times 10^{13}$ W cm^{-2} (absorbed fluence $F_{abs} = 0.098$ J cm^{-2}) the ablation starts and the thin layer of $\approx$50 nm thickness is spalled off from the target, see Fig. 2. Here in time–space coordinates, the evolution of phase states in the vicinity of water–gold interface is presented. Unlike the LA in vacuum, the deceleration of the ablated layer by water is observed. Material spallation occurs at the liquid–solid boundary, where the spall strength is lower than that in the solid phase but the tensile wave is strong enough to cause the cut-off in the liquid phase according to the applied criteria of nucleation.[27] To better understand this process we plot the corresponding thermodynamic trajectories for material layers initially located at depths of 0.5, 11, 21.6, and 30.4 nm under the surface of the target (see Fig. 3).

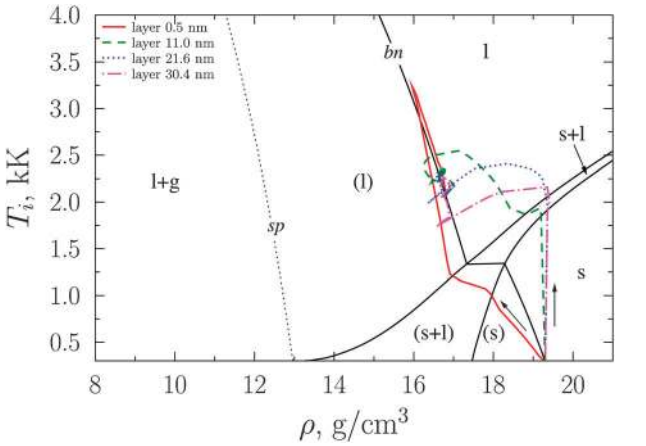

Fig. 3 Fragment of phase diagram with trajectories of gold layers for different initial depths: solid (red)—0.5 nm, dashed (green)—11 nm, dotted (blue)—21.6 nm, dash-and-dot (purple)—30.4 nm. Arrows along the trajectories show the time direction. The local peak intensity on the target is $I_0 = 2 \times 10^{13}$ W cm^{-2}. Denotations of phase states are the same as in Fig. 1.

The thermodynamic paths of ionic component show the consecutive processes of isochoric heating, melting and expansion that eventually results in the spallation of a thin layer. This ablated layer pushes water ahead and the pressure in it increases resulting in the deceleration of the layer by delay $t \approx 2$ ns (Fig. 2).

For the local laser intensity of $I_0 = 3 \times 10^{13}$ W cm^{-2} (absorbed fluence $F_{abs} = 0.26$ J cm^{-2}) we observe a thicker ablated layer of about 200 nm (Fig. 4). Initially, the ablated material consists of several layers but by the delay of $t \approx 3$ ns all of these layers have merged into one thick layer because of the deceleration of the forward layers in water. The corresponding thermodynamic trajectories enter into the metastable liquid region [region (l) in Fig. 5], where the spallation process is followed by the relaxation to the 0 GPa pressure value. Analysis of the thermodynamic path of the front target layer of 0.5 nm [solid (red) curve in Fig. 5] reveals several stages of matter evolution. The first important point, A_1, at this curve is in the metastable liquid phase (close to the spinodal) and is achieved at the moment $t = 0.95$ ps when the pressure of

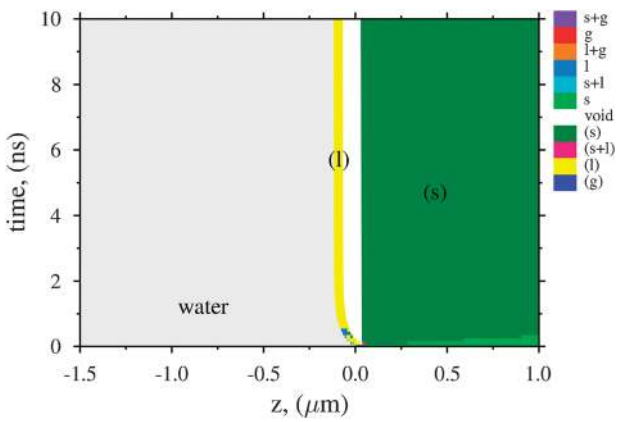

Fig. 2 Time–space diagram of water and gold evolution with phase states for the target material. The local peak intensity of the pulse is $I_0 = 2 \times 10^{13}$ W cm^{-2}. The integral absorption coefficient is $A = 0.023$.

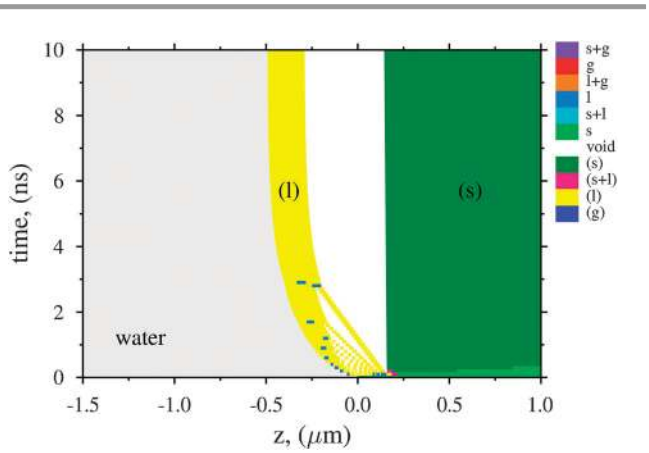

Fig. 4 The same as Fig. 2 but for the local peak intensity $I_0 = 3 \times 10^{13}$ W cm^{-2}. The integral absorption coefficient is $A = 0.04$.

This journal is © the Owner Societies 2013

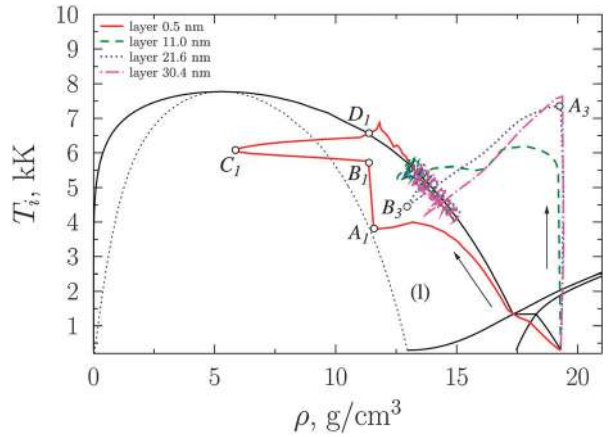

Fig. 5 The same as Fig. 3 but for the local peak intensity $I_0 = 3 \times 10^{13}$ W cm^{-2}. Arrows along the trajectories show the time direction. Thermodynamic parameters at points specified on solid (red) curve: A_1 [t = 0.95 ps, T_i = 3.8 kK, T_e = 21.2 kK, P_i = −5.2 GPa, P_e = 13.7 GPa]; B_1 [t = 1.04 ps, T_i = 5.8 kK, T_e = 20.6 kK, P_i = 0.06 GPa, P_e = 12.8 GPa]; C_1 [t = 6.6 ps, T_i = 6.1 kK, T_e = 10.3 kK, P_i = 0.09 GPa, P_e = 2.23 GPa]; D_1 [t = 17.9 ps, T_i = 6.5 kK, T_e = 6.3 kK, P_i = 0.15 GPa, P_e = 1.25 GPa]. Thermodynamic parameters at points specified on the dotted (blue) curve: A_3 [t = 5.3 ps, T_i = 7.4 kK, T_e = 10.8 kK, P_i = 31.6 GPa, P_e = 4.9 GPa]; B_3 [t = 25.9 ps, T_i = 4.5 kK, T_e = 4.9 kK, P_i = −2.8 GPa, P_e = 0.8 GPa].

ionic subsystem has its minimum P_i = −5.2 GPa. One can expect material spallation to occur long before this moment but it is not the case because the total pressure at this point is positive $P_i + P_e \approx 8.5$ GPa (P_e = 13.7 GPa) due to the thermal non-equilibrium $T_e \gg T_i$. Thus, the thermodynamic instability in the vicinity of the spinodal exponentially increases and fast decay of matter to a new liquid–gas mixture state occurs. See point B_1 in Fig. 5. The ionic temperature and pressure increase abruptly in this process ($\Delta T_i \approx 2$ kK and $\Delta P_i \approx 5.2$ GPa) and the recurrent expansion of the layer starts. Nevertheless, this process stops at point C_1 where the pressures of gold layer and ambient water become equal. Further, the electronic subsystem continues to cool down and the entire pressure in the layer lessens, resulting in initiation of the compression process. Final transformation of the liquid–gas mixture happens at point D_1 where the layer is in the liquid state again.

For a deeper trajectory of 21.6 nm [see dotted (blue) curve in Fig. 5] we observe three noticeable stages: (1) the ultrafast isochoric heating up to point A_3; (2) material rarefaction until spallation at point B_3, where the total pressure is negative ≈ -2 GPa (P_i = −2.8 GPa, P_e = 0.8 GPa); (3) relaxation to zero pressure isobar accompanied by attenuation of multiple acoustic oscillations. As all trajectories enter the metastable liquid region far from the critical point (CP), explosive boiling is not observed. In the regime of ''low-intensity'' pulses we can thus expect the production of large-size population of NPs from the melted ablated layer. Although our simulation is one-dimensional, we can try to estimate the size distribution of NPs originated from the liquid layer fragmentation. As one can see in Fig. 4 the removed material at the early stage $t \lesssim 1$ ns consists of several layers with characteristic thicknesses in the range of 10–40 nm. We expect that these thin layers in the 3D case undergo an instability due to the surface tension work and

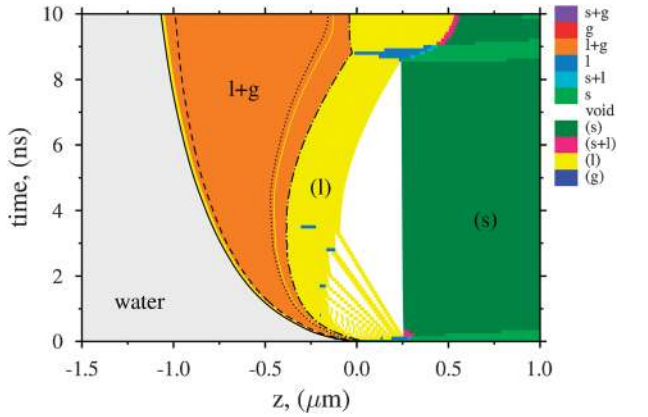

Fig. 6 The same as Fig. 2 but for the local peak intensity $I_0 = 4 \times 10^{13}$ W cm^{-2}. Trajectories correspond to layers: solid—0.5 nm; dashed—11.0 nm; dotted—21.6 nm; dash-and-dot—30.4 nm. The integral absorption coefficient is A = 0.065.

collapse into NPs of a similar size distribution (tens of nanometers), comparable with the experimental findings.[31]

Qualitative changes in the ablation dynamics occur at the further increase of the laser intensity. For the local laser intensity of $I_0 = 4 \times 10^{13}$ W cm^{-2} (absorbed fluence F_{abs} = 0.55 J cm^{-2}) we observe the appearance of a new liquid–gas phase [region l + g (orange) in Fig. 6]. The thickness of the ablated layer is about 250 nm in this case, and the forward target layers undergo explosive boiling when reaching the state with the near CP parameters (see trajectories 11 and 21.6 nm in Fig. 7). In this case, we observe the fast spread of the liquid–gas zone because the pressure in the substance sharply increases at evaporation. This is the reason for fast deceleration of the ablated liquid stratum which is finally turned back to the target. The hot ablated liquid layer enters into contact with the

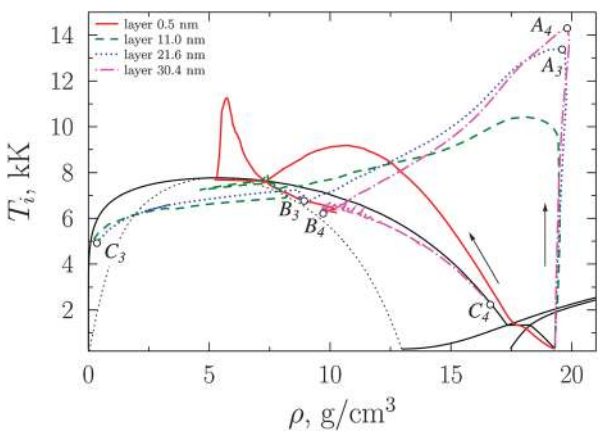

Fig. 7 The same as Fig. 3 but for the local peak intensity $I_0 = 4 \times 10^{13}$ W cm^{-2}. Arrows along the trajectories show the time direction. Thermodynamic parameters at points specified on the dotted (blue) curve: A_3 [t = 5 ps, T_i = 13.5 kK, T_e = 20.9 kK, P_i = 52.7 GPa, P_e = 18.1 GPa]; B_3 [t = 132 ps, T_i = 6.6 kK, T_e = 6.6 kK, P_i = −0.56 GPa, P_e = 1.2 GPa]; C_3 [t = 10 ns, T_i = 4.9 kK, T_e = 4.2 kK, P_i = 0.02 GPa, P_e = 0.03 GPa]. Thermodynamic parameters at points specified on dash-and-dot (purple) curve: A_4 [t = 7 ps, T_i = 14.3 kK, T_e = 18.0 kK, P_i = 58.3 GPa, P_e = 13.5 GPa]; B_4 [t = 48 ps, T_i = 6.1 kK, T_e = 7.2 kK, P_i = −1.2 GPa, P_e = 1.5 GPa]; C_4 [t = 10 ns, T_i = 2.3 kK, T_e = 2.3 kK, P_i = −0.15 GPa, P_e = 0.2 GPa].

target at $t \approx 8.5$ ns resulting in extra melting of the target reaching up to 500 nm depth (see Fig. 6 for the delay $t \gtrsim 9$ ps). Typically, the mean density of the liquid–gas mixture is an order or two less than that for the liquid phase while the temperature in it is higher. For this reason one can expect that smaller particles originate from the liquid–gas region [l + g (orange) zone in Fig. 6] while bigger NPs come from the melted perturbed layer [metastable liquid (l) zone, (yellow) in Fig. 6]. A similar situation with bimodal distribution of NPs was previously observed in experiment.[31–34] The formation of the liquid–gas mixture is clearly seen for the thermodynamic trajectories in Fig. 7 that enter into the metastable liquid region in the vicinity of CP (trajectories 11.0 and 21.6 nm). For the layer 21.6 nm [dotted (blue) curve] one can observe that after isochoric heating (point A_3) the material expansion starts from the pressure $P \approx 70$ GPa until point B_3. At this point the explosive boiling of the homogeneous phase occurs and further rarefaction takes place in the liquid–gas state. Eventually, point C_3 is reached and the balance between gas f_g and liquid f_l volume fractions in it can be calculated using the Maxwell rule giving the ratio $f_g/f_l \approx 42$.

The other dynamics is observed for the layer that was initially at a depth of 30.4 nm. The thermodynamic trajectory of this layer goes through a point of maximum heating A_4, turning point B_4 and point of final relaxation C_4 located at the zero-pressure isobar. This layer is close to the interface between the condensed phase and the liquid–gas mixture (see dash-and-dot curve in Fig. 6).

Finally, the local laser intensity of $I_0 = 5 \times 10^{13}$ W cm^{-2} (absorbed fluence $F_{abs} = 0.95$ J cm^{-2}) leads to a more pronounced evaporation of the target. As a result, the ablated material turns back already by the moment $t \approx 5$ ns (see Fig. 8). The extent of the rarefied liquid–gas mixture is about 1.3 μm towards the end of the process. Since the mass of matter in this phase grows with the laser intensity increase, one can expect an increase of small NP fraction in the solution. The trajectory 30.4 nm demonstrates a sophisticated behavior of matter. The intensive laser heating of the skin layer results in formation of the shock wave that moves into the target and causes the compression of

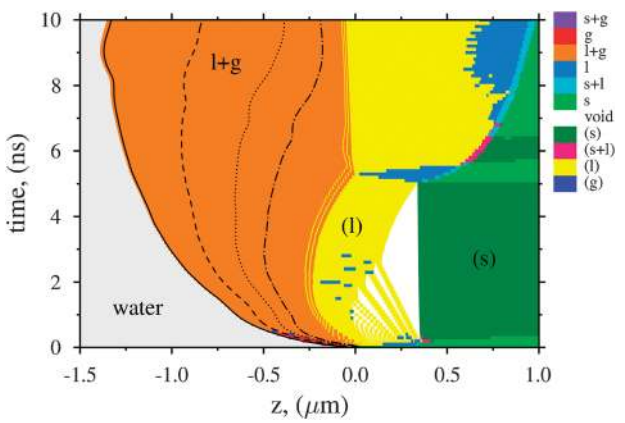

Fig. 8 The same as Fig. 2 but for the local intensity $I_0 = 5 \times 10^{13}$ W cm^{-2}. Trajectories correspond to layers: solid—0.5 nm; dashed—11.0 nm; dotted—21.6 nm; dash-and-dot—30.4 nm. The integral absorption coefficient is $A = 0.089$.

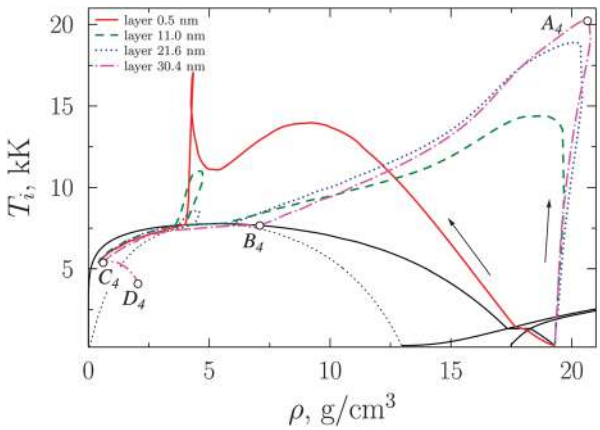

Fig. 9 The same as Fig. 3 but for the local peak intensity $I_0 = 5 \times 10^{13}$ W cm^{-2}. Arrows along the trajectories show the time direction. Thermodynamic parameters at points specified on dash-and-dot (purple) curve: A_4 [t = 6 ps, T_i = 20.7 kK, T_e = 27.4 kK, P_i = 85.6 GPa, P_e = 31.8 GPa]; B_4 [t = 64 ps, T_i = 7.7 kK, T_e = 9.6 kK, P_i = 0.5 GPa, P_e = 2.1 GPa]; C_4 [t = 7.4 ns, T_i = 5.4 kK, T_e = 4.5 kK, P_i = 0.04 GPa, P_e = 0.07 GPa]; D_4 [t = 10 ns, T_i = 3.6 kK, T_e = 3.1 kK, P_i = 0.0 GPa, P_e = 0.1 GPa].

internal layers [see deflection of dash-and-dot (purple) curve from isochor in Fig. 9 during the heating from the initial state to point A_4]. Then, after expansion from this point the phase transition into liquid–gas mixture happens at point B_4, and after that the trajectory reaches point C_4 with minimum density $\rho \approx 0.65$ g cm^{-3}. From the moment 5 ns, the temperature and the pressure in the liquid–gas mixture start to drop more intensively because the hot ablated layer comes into contact with the cold solid target. The layers of the liquid–gas mixture [l + g (orange) area in Fig. 8] nearest to the target start to move in the target direction under the action of the higher external pressure. Close inspection of the trajectory 30.4 nm (dash-and-dot curve in Fig. 8) starting from the moment $t \approx 7$ ns reveals that it comes closer to the target and thus the density in this region grows. Simultaneous cooling and compression processes create favorable conditions for condensation of small NPs in the liquid–gas mixture. As we do not apply a kinetic model to track the liquid–gas mixture evolution starting from point B_4, the information about the size of droplets for this trajectory is lost. Nevertheless, for supercritical trajectories for layers of 0.5, 11.0, and 21.6 nm (see trajectories in Fig. 10) one can estimate the characteristic size of NPs based on a condensation model of Frenkel[35] previously used to calculate the critical droplet size in overcooled gas.[36] Let us consider this process by the example of the trajectory of 11.0 nm (see Fig. 10). Entering into the metastable gas region at point A_2 the supersaturation degree of matter grows. As the trajectory reaches the spinodal at point B_2 the fast transition to a new state (point C_2) with formation of droplets takes place. One can write the balance between a small droplet and supersaturated gas as follows:[35]

$$T_{bn} - T_g = \frac{2\sigma T_{bn} M}{\rho_l U r_{cr}}.$$

Here, T_g is the temperature of supersaturated gas, and T_{bn} is the temperature on binodal at the same density; $\sigma(T)$ is the surface tension; M is the molar mass; ρ_l is the droplet density;

 This journal is © the Owner Societies 2013

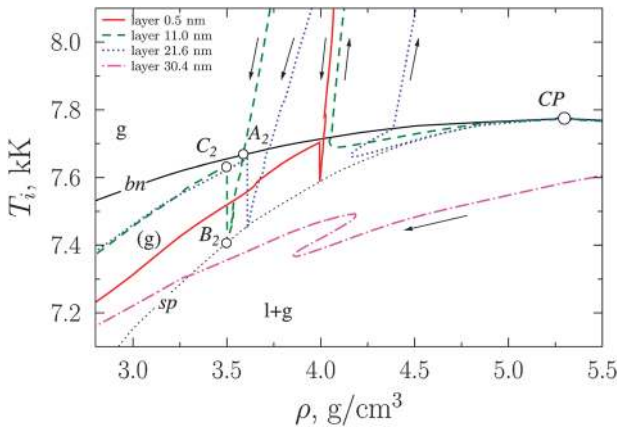

Fig. 10 Zoom of Fig. 9 near the *CP*. Arrows along the trajectories show the time direction. Thermodynamic parameters at points specified on dashed (green) curve: A_2 [t = 420.5 ps, T_i = 7.66 kK, T_e = 7.6 kK, P_i = 0.49 GPa, P_e = 0.9 GPa]; B_2 [t = 507.4 ps, T_i = 7.4 kK, T_e = 7.4 kK, P_i = 0.42 GPa, P_e = 0.83 GPa]; C_2 [t = 508.0 ps, T_i = 7.63 kK, T_e = 7.4 kK, P_i = 0.47 GPa, P_e = 0.83 GPa]. Denotations of phase states are the same as in Fig. 1. The integral absorption coefficient is A = 0.089.

$U(T)$ is the heat of vaporization; r_{cr} is the critical radius of the droplet. Then, we know the temperature at point B_2 ($T \approx$ 7.4 kK) and the surface tension of liquid gold at this temperature can be estimated using linear extrapolation[37] as $\sigma \approx 0.3$ N m^{-1}. From the EOS we calculate the droplet density in the liquid branch of binodal for $T \approx 7.4$ kK as $\rho_l \approx 8.7$ g cm^{-3}; the heat of vaporization at this temperature according to the EOS data is $U \approx 120$ kJ mol^{-1}. It gives an evaluation of the critical droplet radius as $r_{cr} \approx 3.3$ nm that is in a reasonable agreement with experimental observations of "small-size" NP distribution.[6]

Fabbro *et al.* previously investigated the laser ablation under strong confinement[14,38] and demonstrated that the ablation threshold was larger in this case than in vacuum because of the strong pressure, which prevented target expansion. We also compare the results for ablation into liquid with ones obtained under vacuum for the same local laser intensity (see Fig. 8 and 11). As one can see in Fig. 11 the ablated fragments of the target moves with high speed and the layers originated from the melted stratum have similar size distribution of tens of nanometers. The basic difference is in the characteristic length of the liquid–gas mixture area which has an extent of about 40 μm for ablation into vacuum (~1.4 μm in presence of water) and thus the much lower density. The later factor can result in other distributions of "small-size" population of NPs but additional kinetic models of condensation and coagulation are required to address this issue.

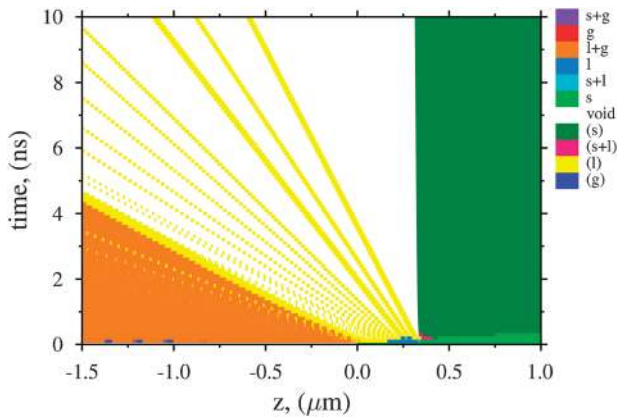

Fig. 11 Time–space diagram of gold target ablation into vacuum for laser peak intensity $I_0 = 5 \times 10^{13}$ W cm^{-2}.

4 Summary

For simulation of multi-stage processes of femtosecond laser ablation of gold target into ambient water we develop the two-temperature wide-range hydrodynamic model. It consistently describes the laser energy absorption, thermal conduction, electron–phonon/ion coupling, material expansion and compression. For the description of thermodynamic functions of gold we use thermodynamically complete multi-phase EOS with stable and metastable phases. Usage of this EOS enables us to describe phase transitions as well as introduce kinetics for the evolution of the metastable liquid state.

It is shown in numerical simulations that the large-size particles are the result of liquid layer ejection and fragmentation. This regime is observed for low laser intensities when the thermodynamic trajectories enter the metastable liquid region far below the CP. For higher laser intensities, the near-critical and supercritical trajectories appear for front target layers and the mass fraction of the liquid–gas mixture increases. Formation of small NPs can be observed for these trajectories and estimation of the NPs size matches quite well with the experimental findings. The calculation results thus explain bimodal size distributions of NPs frequently observed in experiment. For an accurate description of NP formation and evolution in supersaturated gas and liquid–gas mixtures, additional models should be developed.

Acknowledgements

France–Russia collaboration supported by French CNRS and Russian Academy of Sciences and the CINES of France for computer time under the project number C2012085015. This work was also supported by the Russian Foundation for Basic Research (project nos. 11-08-01225, 13-08-01179 and 13-02-91057).

References

1 J. S. Bradley, G. Schmid, D. V. Talapin, E. V. Shevchenko and H. Weller, *Syntheses and Characterizations 3.2 Synthesis of Metal Nanoparticles*, Wiley-VCH Verlag GmbH & Co. KGaA, 2005, pp. 185–238.
2 A. V. Simakin, E. N. Lubnin and G. A. Shafeev, *Quantum Electron.*, 2000, **30**, 263.
3 G. Yang, *Prog. Mater. Sci.*, 2007, **52**, 648–698.
4 F. Mafuné, J.-y. Kohno, Y. Takeda and T. Kondow, *J. Phys. Chem. B*, 2003, **107**, 12589–12596.

5 A. V. Kabashin and M. Meunier, *J. Phys. Conf. Ser.*, 2007, **59**, 354.
6 A. V. Kabashin and M. Meunier, *J. Appl. Phys.*, 2003, **94**, 7941–7943.
7 R. Thareja and S. Shukla, *Appl. Surf. Sci.*, 2007, **253**, 8889–8895.
8 K. Niu, J. Yang, S. A. Kulinich, J. Sun, H. Li and X. W. Du, *J. Am. Chem. Soc.*, 2010, **132**, 9814–9819.
9 T. E. Itina, *Chem. Phys. Lett.*, 2008, **452**, 129–132.
10 T. E. Itina, K. Gouriet, L. V. Zhigilei, S. Noël, J. Hermann and M. Sentis, *Appl. Surf. Sci.*, 2007, **253**, 7656–7661.
11 L. V. Zhigilei and B. J. Garrison, *J. Appl. Phys.*, 2000, **88**, 1281–1298.
12 I. Ozerov, D. Nelson, A. Bulgakov, W. Marine and M. Sentis, *Appl. Surf. Sci.*, 2003, **212–213**, 349–352.
13 A. V. Gusarov, A. G. Gnedovets and I. Smurov, *J. Appl. Phys.*, 2000, **88**, 4352–4364.
14 R. Fabbro, P. Peyre, L. Berthe and X. Scherpereel, *J. Laser Appl.*, 1998, **10**, 265.
15 J. Park, V. Privman and E. Matijevic, *J. Phys. Chem. B*, 2001, **105**, 11630–11635.
16 M. E. Povarnitsyn, N. E. Andreev, P. R. Levashov, K. V. Khishchenko and O. N. Rosmej, *Phys. Plasmas*, 2012, **19**, 023110.
17 C. H. Fan, J. Sun and J. P. Longtin, *J. Appl. Phys.*, 2002, **91**, 2530–2536.
18 A. Menéndez-Manjón, P. Wagener and S. Barcikowski, *J. Phys. Chem. C*, 2011, **115**, 5108–5114.
19 M. Born and E. Wolf, *Principles of optics*, Cambridge University Press, 7th edn, 1999.
20 M. E. Povarnitsyn, N. E. Andreev, E. M. Apfelbaum, T. E. Itina, K. V. Khishchenko, O. F. Kostenko, P. R. Levashov and M. E. Veysman, *Appl. Surf. Sci.*, 2012, **258**, 9480–9483.
21 *Handbook of Optical Constants of Solids I*, ed. E. D. Palik, Academic Press, 1985.
22 L. Spitzer and R. Härm, *Phys. Rev.*, 1953, **89**, 977–981.
23 E. M. Apfelbaum, *Phys. Rev. E: Stat., Nonlinear, Soft Matter Phys.*, 2011, **84**, 066403.
24 Z. Lin, L. V. Zhigilei and V. Celli, *Phys. Rev. B: Condens. Matter Mater. Phys.*, 2008, **77**, 075133.
25 O. P. Shemyakin, P. R. Levashov, L. R. Obruchkova and K. V. Khishchenko, *J. Phys. A: Math. Theor.*, 2010, **43**, 335003.
26 M. E. Povarnitsyn, T. E. Itina, M. Sentis, P. R. Levashov and K. V. Khishchenko, *Phys. Rev. B: Condens. Matter Mater. Phys.*, 2007, **75**, 235414.
27 M. E. Povarnitsyn, K. V. Khishchenko and P. R. Levashov, *Appl. Surf. Sci.*, 2009, **255**, 5120–5124.
28 I. V. Lomonosov, V. E. Fortov and K. V. Khishchenko, *Chem. Phys. Rep.*, 1995, **14**, 51–57.
29 *LASL Shock Hugoniot Data*, ed. S. P. Marsh, University of California Press, Berkeley, 1980, p. 680.
30 L. P. Volkov, N. P. Voloshin, R. A. Mangasarov, V. A. Simonenko, G. V. Sin'ko and V. L. Sorokin, *J. Exp. Theor. Phys. Lett.*, 1980, **31**, 513–515.
31 J.-P. Sylvestre, A. Kabashin, E. Sacher and M. Meunier, *Appl. Phys. A: Mater. Sci. Process.*, 2005, **80**, 753–758.
32 A. Menéndez-Manjón and S. Barcikowski, *Appl. Surf. Sci.*, 2011, **257**, 4285–4290.
33 L. Lavisse, J.-L. L. Garrec, L. Hallo, J.-M. Jouvard, S. Carles, J. Perez, J. B. A. Mitchell, J. Decloux, M. Girault, V. Potin, H. Andrzejewski, M. C. M. de Lucas and S. Bourgeois, *Appl. Phys. Lett.*, 2012, **100**, 164103.
34 S. Ibrahimkutty, P. Wagener, A. Menzel, A. Plech and S. Barcikowski, *Appl. Phys. Lett.*, 2012, **101**, 103104.
35 J. Frenkel, *Kinetic Theory of Liquids*, Oxford University Press, Oxford, 1946, p. 544.
36 E. Lescoute, L. Hallo, D. Hébert, B. Chimier, B. Etchessahar, V. T. Tikhonchuk, J.-M. Chevalier and P. Combis, *Phys. Plasmas*, 2008, **15**, 063507.
37 I. Egry, G. Lohoefer and G. Jacobs, *Phys. Rev. Lett.*, 1995, **75**, 4043–4046.
38 L. Berthe, R. Fabbro, P. Peyre, L. Tollier and E. Bartnicki, *J. Appl. Phys.*, 1997, **82**, 2826–2832.

 This journal is © the Owner Societies 2013